Research Square

Preprints are preliminary reports that have not undergone peer review.
They should not be considered conclusive, used to inform clinical practice,
or referenced by the media as validated information.

Multi-Mode Droplet Splitting on Active-Matrix Digital Microfluidics: Quantitative Boundaries and Optimal Sequential Generation

Hanbin Ma

hanbin.ma@uestc.edu.cn

University of Electronic Science and Technology of China https://orcid.org/0000-0002-7629-2287

Chenxuan Hu

University of Electronic Science and Technology of China

Article

Keywords:

Posted Date: May 13th, 2026

DOI: https://doi.org/10.21203/rs.3.rs-9577238/v1

License: This work is licensed under a Creative Commons Attribution 4.0 International License.
Read Full License

Additional Declarations: There is no conflict of interest

Version of Record: A version of this preprint was published at Microsystems & Nanoengineering on September 28th, 2026. See the published version at https://doi.org/10.1038/s41378-026-01433-8.

Abstract

Precise generation of microdroplets at picoliters to microliters scale is critical for advancing microfluidics technologies and precision life sciences research. Digital microfluidics enables programable individual droplet, however, there still lacks comprehensive characterization and analysis on optimal splitting modes, hindering its further application requiring extreme volume accuracy and splitting. Here, we report a systematic quantitative investigation of four droplet splitting strategies: symmetric splitting, asymmetric splitting, deformative splitting, squeezing, leveraging the high programmability advantage of large-scale active-matrix digital microfluidics. Droplet splitting is experimentally tested across varying droplet sizes, shapes, ratios and sub-droplet motion modes. Based on extensive experimental results, quantitative analysis is conducted to comprehensively characterize the splitting accuracy and effective ratio ranges. From these statistical results and optimal splitting modes, we establish an optimal sequential splitting decision framework. Aiming at precise generation for ultra-low-ratio sub-droplet through sequential splitting, the proposed framework can efficiently screen reasonable splitting paths from the combinatorial solution space. Ultra-low-ratio droplet generation at 0.78125% is realized, which is unattainable by any single-step method, with a cumulative accuracy of 1.05868 upon a target droplet of 12nL. This work clarifies the quantitative performance boundaries of multi-type droplet splitting strategies and demonstrates the capability of standardized optimal splitting sequence generation. These findings provide a theoretical and technical basis for customized multi-step droplet preparation and high-stability microfluidic manipulation.

Introduction

Microfluidics[1], also known as lab-on-a-chip systems, have emerged as powerful and miniaturized analytical platforms and are widely deployed in advanced research fields, including precision biomedical analysis, high-throughput biochemical reaction, and single-cell analysis[2, 3]. To achieve controllable microdroplet generation, diverse microfluidic manipulation strategies based on different physical and structural principles have been widely developed and investigated, including passive microfluidics[4] and active microfluidics[5]. However, most microfluidic platforms are constrained by fixed structural dimensions, which severely limit the adjustable range of generated droplet sizes and restrict flexible droplet manipulation[6]. With the rapid development of high-precision biochemical experiments and complex microscale reaction systems, advanced research has put forward requirements for droplet volume consistency and accuracy[7–9]. Furthermore, such platforms are difficult to integrate with downstream reaction processes involving complex reagents and fluids.

To address these challenges, electrowetting-on-dielectric (EWOD)-based digital microfluidics (DMF)[10] has emerged as a highly programmable platform that enables individual control over each droplet[11, 12], rendering it promising for complex biological and chemical applications[13, 14]. Despite advances in DMF-based droplet generation, bio-applications requiring extreme volume accuracy and splitting resolution remain challenging. Existing studies lack systematic quantitative characterization of diverse splitting modes for optimal sub-droplet generation. Investigation on optimal splitting modes is further

hindered by high chip costs and rigid electrode structure designs. This limitation is inherent to conventional DMF chips. Restricted by the hardware driving system, typical DMF devices contain no more than 200 electrodes, resulting in highly constrained electrode array layouts and electrode dimension designs. Furthermore, due to the physical limitations of droplet actuation (i.e., the aspect ratio limit), individual electrodes are relatively large, and droplet volumes typically remain at the microliter level. Consequently, it is nearly infeasible to experimentally conduct droplet generation mode tests across a broad size range on such a restricted electrode array, let alone to systematically validate droplet generation accuracy, strategies, and motion modes.

To overcome the limitations in droplet control throughput and precision, the active-matrix digital microfluidics (AM-DMF) approach offers a promising solution. AM-DMF chip design leverages large-area thin-film electronics technology[15, 16], enabling the fabrication of chips with large-area electrode arrays. It makes it possible to characterize and test the dynamic splitting performance of droplets across a wide volume range based on matrix operations [17, 18]. Droplet splitting strategies, such as continuous “one-to-two”[19] and “one-to-three”[20] have been successfully demonstrated on such platforms.

Here, we report a systematic quantitative data investigation of diverse droplet splitting behaviors for precise sub-droplet splitting and generation. This study is based on comprehensive quantitative testing and data analysis of four typical droplet splitting modes, implemented on the programmable large-scale AM-DMF platform. Compared with conventional microfluidic strategies that merely focus on fixed splitting operations and qualitative phenomenon observation, this work prioritizes systematic data acquisition and quantitative characterization of the performance boundaries, including splitting accuracy, splitting ratio limitation, sub-droplets motion modes and cumulative error rules for different splitting methods. Furthermore, a constraint-driven optimal splitting decision framework is constructed to validate the obtained quantitative data conclusions. The inherent quantitative laws of multi-mode droplet splitting are validated, confirming that optimal splitting paths enable high-precision, customizable multi-step droplet generation. The work is promising for guiding DMF electrode array design and highly precise microdroplet generation.

Results

Overview of precise droplet splitting studies on the AM-DMF platform

Four DMF-based sub-droplet generation strategies are proposed and analyzed to address the core problem of precise droplet control (Fig. 1). The programmable AM-DMF chip featured a multilayer architecture with 16,384 independently programmable electrodes, enabling nanolitre-scale droplet control and activated by a core control board (Fig. 1a). Droplet splitting performance and sub-droplet morphologies are captured by a camera and measured in image processing software. Droplet actuation voltage is set as 30V. Distilled water is used for droplet generation.

In double-plate structure digital microfluidics, a droplet can be approximated as a cylinder with a very small height. Due to wetting effects, the advancing and receding contact angles of the droplet differ, resulting in non-uniform upper and lower surface areas of the cylinder. However, when the droplet is sufficiently large and the advancing contact area accounts for a relatively small proportion, it can be simplified as an ordinary cylinder. In such cases, within the same DMF chip, droplet volume changes are simplified to area changes on the electrode plane. This simplification hypothesis is adopted in this work.

Four droplet splitting strategies: symmetric splitting, asymmetric splitting, deformative splitting, squeezing, are proposed and analyzed (Fig. 1b). Although previous studies have fully demonstrated the feasibility of single-electrode droplet splitting on the present chip platform, potential test errors arising from variations in control capability among individual electrodes cannot be overlooked. To minimize such errors, the minimum width and length for droplet deformation and splitting were both constrained to two electrode units in this study. Furthermore, each experimental condition was tested at least three times to enable analysis of intra-group splitting stability.

(a) System setup, chip structure and optical detection images. (b) Schematic of four different droplet splitting strategies on AM-DMF (symmetric splitting, asymmetric splitting, deformative splitting, squeezing). A framework for optimal target droplet splitting decision is also established.

Symmetric droplet splitting

In our previous work, the strategy was proposed as an efficient method for sequential droplet generation[19], and validated through theoretical calculations and simulations. To further investigate sub-droplets volume accuracy under symmetric splitting, analysis is extended to the effects of initial droplet size (D = w l), initial droplet shape (defined by the deformation factor R = w/l), and sub-droplets motion modes (Dm_1, Dm_2) (Fig. 2). The droplet splits along the direction perpendicular to its width. The horizontal motion of sub-droplets in opposite directions is described by the vector components. It should be emphasized that the term "motion" here does not refer to measured velocity, given that droplet speed is not constant during the splitting and movement processes. The present work focuses exclusively on direction. The absolute values indicate step sizes: a value of 1 corresponds to one electrode per step (125 μm), and a value of 2 corresponds to two electrodes per step (250 μm). For an initial droplet D, two sub-droplets $D_1 = w_1$ l, $D_2 = w_2$ l, and $w_1 = w_2$=w/2 (Fig. 2a). The initial droplet closely resembles a square when initial droplet deformation factor R = 1, elongated when R < 1, compressed when R > 1. Experimental images show symmetric splitting of an initial droplet (D = 256) into sub-droplets with varying shapes (R < 1, R = 1, R > 1) (Fig. 2b). Scale bar is 1mm, with a single electrode pitch of 125 μm.

Figure 2c shows the sub-droplets accuracies under four motion modes (Dm_1, Dm_2) = (0,1), (-1,1), (0,2), (-2,2). These data points were obtained from initial droplets spanning a range of sizes (D = 64 to 1024, droplet volume 200nL to 3.2 μL) and shape factors (R = 0.0625 to 16). The x axis corresponds to D, and the y-axis corresponds to R, with the ranges as indicated. The coordinates are plotted on a lg-lg scale. For each experimental condition, the accuracy Acc. is defined as the normalized mean relative volume of

both sub-droplets. The overall Acc. ranges from 1.04 to 1.2. In the bubble plots, the bubble diameter is linearly proportional to accuracy. Thus, a decreasing bubble size denotes increasing accuracy. The intra-group standard deviation ranges from 0 to 0.01. It is encoded by bubble color gradient from deep red to deep blue, where a progressive decrease in hue indicates enhanced data consistency. The overall bubble distribution, mapped on a blue gradient background, indicates a trend of enhanced sub-droplets accuracy with increasing D and increasing R. The maximum error, represented by the largest bubble size, is observed at the smallest initial droplet size (D = 64, droplet volume 200 nL). As D increases, the error progressively diminishes. When D exceeds 512, the bubble size becomes extremely small and difficult to resolve visually.

The average accuracies for four motion modes decrease in the following order: (Dm_1, Dm_2) = (-1,1), 1.03095, (Dm_1, Dm_2) = (0,1), 1.04339, (Dm_1, Dm_2) = (-2,2), 1.0592, (Dm_1, Dm_2) = (0,2) ,1.04771. The results demonstrated that symmetric motion states with opposite directions, specifically (-1,1) and (-2,2), enhance splitting accuracy, with (-1,1) yielding the highest accuracy. Meanwhile, motion modes (-2,2) and (0,2) perform worse than (-1,1) and (0,1), indicating that a lower step velocity (i.e., one electrode per step rather than two) improves droplet splitting accuracy. Furthermore, the bubble color distribution indicates that data consistency also performs the best when for (-1,1), with all intra-group standard deviation below 0.005. This improvement is particularly pronounced at the minimum droplet size (D = 64), where motion mode (-1,1) significantly enhanced both splitting accuracy and consistency. Therefore, the motion mode (Dm_1, Dm_2) = (-1,1) yields optimal performance in both accuracy and data consistency.

To further investigate the factors affecting sub-droplet splitting accuracy and consistency under the motion mode (Dm_1, Dm_2) = (-1,1), a box plot is employed in Fig. 2d to facilitate quantitative comparison across conditions. Three representative initial droplet sizes D = 64, 256 and 1024 are examined. At an initial droplet shape of R = 0.0625, the accuracy exhibits unsatisfactory values of 1.49808 for D = 256 and 1.33141 for D = 1024, suggesting the existence of a minimum feasible R for droplet deformation. As D increases from 64 to 256 and 1024, an upward trend in accuracy is observed. To enable precise analysis at R = 0.25, 1, and 4, the range is confined to 1.0 to 1.15. Across the three D values, accuracy increases monotonically with R, accompanied by enhanced intra-group data consistency. For D = 256 and R ≥ 0.25, accuracy error remains within the 5% limit. For D = 1024 and R ≥ 0.25, the error converges to within 2%. The results indicate that uniform symmetric splitting is enhanced when the initial droplet is either compressed in shape or larger in size.

(a) Schematic diagram of symmetric splitting. (b) Experimental images of symmetric splitting. Scale bar is 1mm. (c) Experimental results of sub-droplet accuracy at different splitting motion modes (Dm_1, Dm_2), initial droplet size (D = w l) and shape (R = w/l). (d) Sub-droplet accuracies under three typical initial droplet sizes (D = 64, 256, 1024) when motion mode (Dm_1, Dm_2) = (-1,1).

Asymmetric droplet splitting

While symmetric droplet splitting demonstrates high sub-droplet accuracy, it only allows for a fixed splitting ratio of 0.5 in a single split. To enable droplet splitting across a broader range of ratios, asymmetric droplet splitting presents a viable solution (Fig. 3). It was previously proposed for enrichment of rare cells by efficiently isolating them from heterogeneous bulk samples [21]. For initial droplet D = w l, two sub-droplets $D_1 = w_1$ l, $D_2 = w_2$ l, subject to the constraint $w_1 + w_2$=w (Fig. 3a). $w_1 = w_2$ describes the case of symmetric splitting. Experimental images illustrate sub-droplets formation under asymmetric splitting for varying initial droplet shapes (R < 1, R = 1, R > 1, and R > > 1) (Fig. 3b). As the two sub-droplets differ in volume, the target droplet definition varies by motion modes. It is important to recognize that the effect of moving a single sub-droplet depends on which droplet is in motion, owing to their volume disparity. Therefore, the influence of volume should be decoupled from that of motion mode for proper differentiation. The configurations of (-1,0) and (0,1) must be examined separately. Therefore, the target droplet is defined as follows: for (Dm_1, Dm_2) = (-1,0), the moving sub-droplet is the target droplet. For (Dm_1, Dm_2) = (0,1), the stationary sub-droplet is the target droplet. For (Dm_1, Dm_2) = (1,1), both sub-droplets are the target droplets. As lower step motions showcased improved accuracy and consistency in previous section, (0,2) and (-2,2) will not be investigated in afterward sections.

Correlation analysis between the theoretical target droplet ratio (D_{t-theo}=D_{1-theo} /D_{theo}) and the experimental target droplet ratio (D_{t-exp}=D_{1-exp}/$D_{-\ exp}$) is conducted for initial droplet D = 256 (droplet volume 0.8 μL) (Fig. 3c), and D = 1024 (droplet volume 3.2 μL) (Fig. 3e), at three motion modes (Dm_1, Dm_2) = (-1,0), (1,1) and (0,1). The case D_{t-theo}=0.5 corresponds to symmetric splitting. Error bar indicates intra-group deviation. As shown in Fig. 3c and Fig. 3e, the yellow solid line is the reference baseline, defined by D_{t-exp}= D_{t-theo}. Data points distributed below the line indicate undersized target droplets, while those above the line represent oversized target droplets. The correlation diagram shows that, at constant R, theoretical and experimental values converge as D_t increases. At constant Dt, increasing R also improves agreement. Moreover, a larger R lowers the minimum attainable Dt, indicating higher droplet splitting resolution. When D = 256, the minimum attainable D_{t-theo} is 0.03125 when R = 16. It must be clarified that limited by the electrode array scale, R = 16 is beyond measurement for D = 1024, therefore the minimum attainable D_{t-theo} is 0.03125 when R = 4.

Figure 3c indicates that significant volume deviation emerges when D_t falls below 0.1. At D = 256, R = 4, within the D_{t-theo} in the range (0, 0.2), motion mode (-1,0) yields undersized target droplet, while (-1,1) and (0,1) yield oversized target droplet. Figure 3e indicates that At D = 1024, R = 4, under the same shape and within the same D_{t-theo} range (0, 0.2), motion mode (-1,0) yields undersized target droplet, (0,1) yields oversized target droplet, both consistent with the trends observed at D = 256, R = 4. In contrast, mode (-1,1) yields an undersized target droplet, which is opposite to the trend at D = 256, R = 4. Moreover, when D_{t-theo} exceeds 0.2, volume errors are not apparent in the correlation diagram due to the high overall accuracy.

Therefore, a dedicated quantitative analysis of the target droplet volume accuracy is conducted for clear comparison on accuracy and consistency across groups. The absolute value of normalized volume

accuracy $|D_{t-exp}.ND|$ of target droplet D_t under D = 256 and D = 1024 is illustrated (Fig. 3d, Fig. 3f). To exclude the effect of absolute value of D_t, normalized D_{t-exp} is defined as:

$D_{t-exp}.ND$= (average (D_{t-exp})- D_{t-theo})/ D_{t-theo}

Error bars represent the coefficient of variance (CV), defined as the ratio of standard deviation (SD) of experimental value and average experimental value.

CV=stddev (D_{t-exp})/ average (D_{t-exp})

In Fig. 3d and Fig. 3e, the yellow dashed line indicates $D_{t-exp}.ND = 0$, which is equivalent to the yellow solid line in the correlation diagram. The gray dashed line indicates $|D_{t-exp}.ND|=0.1$, defining a 10% accuracy error tolerance. The vertical orange dashed line indicates $D_{t-theo} = 0.5$, representing symmetric splitting. Overall, asymmetric splitting exhibits a higher error compared to symmetric splitting, with an upper error bound of 0.2. $|D_{t-exp}.ND|$ exhibits a decreasing trend at motion mode (-1,0) and (-1,1), while an increasing trend at (0,1). Consistent with the trend observed in symmetric splitting, when D increases from 256 to 1024, the minimum attainable D□ reduces.

In Fig. 3d, the coefficient of variation (CV) and |D□_□□□.ND| vary with D□_□□□□ under different motion modes. For modes (-1,0) and (-1,1), CV decreases as D□_□□□□ increases. For mode (0,1), CV increases when D□_□□□□ approaches 1. When D_{t-theo} ranges from 0.1 to 0.5, it can be observed that $|D_{t-exp}.ND|$ remains below 0.1 for all motion modes. At minimum attainable $D_{t-theo} = 0.03125$ when R = 16, $|D_{t-exp}.ND|$ drops sharply from 0.294, 0.278, and 0.007 for modes (-1,0), (-1,1), and (0,1) respectively. At the second minimum attainable $D_{t-theo} = 0.0625$, when R = 16, the corresponding $|D_{t-exp}.ND|$ are 0.055, 0.190, and 0.015 under (-1,0), (-1,1), and (0,1) respectively; at the same D□_□□□□ when R = 4, $|D_{t-exp}.ND|$ are 0.047, 0.272, 0.015 under (-1,0), (-1,1), and (0,1) respectively. Notably, motion mode (0,1) exhibits exceptional performance in low D_t range. When D_{t-theo} exceeds 0.5, all $|D_{t-exp}.ND|$ is below 0.021 for mode (-1,0), and below 0.028 for mode (-1,1). In contrast, mode (0,1) shows a maximum $|D_{t-exp}.ND|$ of 0.06 for (0,1), indicating increasing volume error at higher D□. Overall, for modes (-1,0) and (-1,1), both CV and |D□_□□□.ND| decrease as D□_□□□□ increases, while for mode (0,1), both metrics increase when D□_□□□□ approaches 1. Therefore, no single motion mode is universally optimal. Mode (0,1) is preferred for ultra-low-ratio sub-droplet splitting with D□ below 0,1. Modes (-1,0) and (-1,1) are more reliable when D□ exceeds 0.5. In the intermediate range when D□ ranges from 0.1 to 0.5, sub-droplets accuracies become insensitive to either motion mode employed. In Fig. 3f, asymmetric splitting on the initial droplet D = 1024 exhibits a similar trend that observed for D = 256 in Fig. 3d. An obvious trend emerges that increasing R leads to a higher minimum D_t and improved accuracy under feasible deformation conditions. When D_{t-theo} is below 0.2, $|D_{t-exp}.ND|$ remains below 0.01 at mode (0,1) under R = 4, indicating an exceptional volume accuracy exceeding 99%.

(a) Schematic diagram of asymmetric splitting. (b) Experimental images of deformative splitting in varying initial droplet shapes. (b) Correlation analysis on initial droplet D = 256 with different shapes R under sub-droplets motion modes (Dm_1, Dm_2) = (-1,0), (-1,1) and (0,1). (c) Correlation analysis on initial droplet sizes D = 256 and (e) D = 1024 with different shapes R under three motion modes. (d) Statistical analysis on the absolute normalized deviation of experimental results of target droplet ratio ($|D_{t_exp}.ND|$) in relation with corresponding theoretical target droplet ratio (D_{t_theo}) under initial droplet sizes D = 256 and (f) D = 1024.

Deformative droplet splitting and squeezing

To generate two sub-droplets from the initial droplet in one split, symmetric splitting and asymmetric splitting showcased excellent performance in sub-droplet volume accuracy. However, their feasibility for advanced requirements is constrained by two limitations: the resolution of minimal target sub-droplet is insufficient for ultra-low-ratio generation, and the high demand on chip electrode array for droplet deformation and low-ratio sub-droplet generation. Recent research has proposed an efficient squeezing method for droplet generation out of a reservoir, enabling target droplet generation of low volume ratios. This approach demonstrated the importance of irregular initial droplet deformation. Motivated by this finding, we propose deformative splitting strategies, with squeezing strategy as a representative example.

The geometries of both target droplet (D_1, R_1) and reservoir droplet (D_2, R_2) and their effects on target droplet accuracy are studied. For initial droplet D = w l, two sub-droplets $D_1 = w_1\ l_1$, $D_2 = w_2\ l_2$. Since deformative strategies focus on achieving high resolution for droplet generation, this section only discusses the volume accuracy of target droplets, without redundant discussion on the accuracy of the reservoir droplets (bigger sub-droplets). To investigate the feasibility of sub-droplet deformation, the circumstance of sub-droplets with equal width $w_1 = w_2 = w/2$ is first studied (Fig. 4). In previous strategies, no deformation occurs in initial rectangular droplets, and the deformation coefficient R is defined as the sum of the sub-droplet widths divided by the droplet height. However, here the two sub-droplets exhibit different heights after deformation. Correspondingly, the deformation coefficient R_d is revised to the sub-droplet width divided by the average height. Given the difference in physical implication compared with the previous definition, to distinguish this parameter from the previous R, this new deformation coefficient is denoted as R_d. Here, $l_1 + l_2 = 2l$, $R_d = w/2(l_1 + l_2)$. The numerical relationship between R and R_d is $R_d = 1/R$. Experimental images show sub-droplets under asymmetric splitting with different shapes (R_d=0.0625, 0.25, 1, 4) (Fig. 3b).

Correlation analysis between theoretical target droplet ratio (D_{t-theo}) and experimental target droplet ratio (D_{t-exp}) is conducted for initial droplet D = 256 (Fig. 4c), under sub-droplet motion modes (Dm_1, Dm_2) = (-1,0), (1,1) and (0,1). In deformative splitting, as R_d decreases, |D□_□□□.ND| increases and the minimum target droplet ratios reduce, indicating enhanced both absolute accuracy and resolution. Given

that R_d=1/R, this trend is consistent with the behavior observed in the previous two splitting strategies (Fig. 4d). Intra-group data consistency is also enhanced significantly compared to previous strategies. The most notable distinction lies in how motion modes affect target droplet accuracy. Specifically, under mode (-1,0), |D□_□□□.ND| increases with D□_□□□□, whereas under modes (-1,1) and (0,1), |D□_□□□.ND| decreases as D□_□□□□ increases. This indicates a trend opposite to that observed in the previous two splitting methods. When R_d=0.0625, D_{t-theo} reaches its minimum of 0.03125 at (-1,1), which is identical to the case of R = 16. However, deformative splitting failed at D_{t-theo}=0.03125. When D□_□□□□= 0.0625, for R_d= 0.0625 and 0.25, the corresponding $|D_{t-exp}.ND|$ are 0.007 and 0.001 under (-1,0), indicating an exceptional volume accuracy exceeding 99.3% and 99.9%. The ideal accuracy and uniformity observed in deformative splitting indicate that pursuing squeezing at even lower volume ratios is meaningful. Nevertheless, in this configuration, the two sub-droplets share an identical width w, which limits the achievable range of volume ratios. When w exceeds a certain threshold, stable droplet deformation is compromised, rendering the elongation and splitting of two compressed sub-droplets challenging. Consequently, investigate squeezing under conditions where neither the width nor the length of the sub-droplets is fixed is investigated in the following section.

(a) Schematic diagram of deformative splitting. (b) Experimental images of deformative splitting in varying R_d. (c) Correlation analysis and on initial droplet sizes D = 256 with varying shapes R_d. at different sub-droplets motion modes (Dm_1, Dm_2) = (-1,0), (-1,1) and (0,1). (d) Statistical analysis on absolute normalized deviation of experimental results of target droplet ratio ($|D_{t_exp}.ND|$) in relation with corresponding theoretical target droplet ratio (D_{t_theo}) when D = 256.

The special circumstance of deformative splitting showcased its potential for droplet deformation-based splitting. The principal focus lies on the resolution breakthrough achieved through the squeezing method. Therefore, a flexible deformative splitting strategy Sis further investigated, referred to as squeezing (Fig. 5). Schematic diagram of squeezing is shown in Fig. 5a. To investigate the lower limit of sub-droplet splitting, target droplets of the ratio D_t%= D_t/ D×100%=1.5625% split from the initial droplet D = 1024 (Fig. 5b) and D = 256 (Fig. 5d), target droplets of D_t%=3.125% split from initial droplet D = 256 (Fig. 5c) and D = 1024 (Fig. 5e) are studied. Owing to the small ratio D_t%, target droplets accuracy is strongly affected by sub-droplet motion modes. The sign of the error indicates whether the target droplet is oversized (positive error) or undersized (negative error). $D_{t-exp}.ND$ of target droplets D_1 for each D_2 at different sub-droplet motion modes are compared, ranging from − 0.5 to 0.5. Corresponding experimental images are attached in each subplot. The blue dashed line indicates $D_{t-exp}.ND$ = 0, functioning as the baseline.

In Fig. 5b, target droplets possess a unified size of D_1 = 16 with three morphologies (2×8, 4×4, 8×2). Reservoir droplets possess a unified size of D_2=1008 with two morphologies (63×16, 16×63). Failed splits occur under D_1 = 8×2 while D_2 = 16×63 at all motion modes, indicating that severe width mismatch prevents successful splitting. Failed splits also occur under D_1 = 4×4 while D_2 = 16×63, and under D_1 =

8×2 and D_2 = 63×16, both only at sub-droplet motion (-1,0). The sign of error is also mode dependent. D_{t-exp}.ND is negative under D_1 = 2×8 while D_2 = 16×63 and D_2 = 63×16 at (-1,0), but positive at (0,1). The highest accuracy and consistency occur under D_1 = 4×4 and D_2 = 63×16 at (-1,0), where $|D_{t-exp}.ND|$=0.047, CV = 0.005, demonstrating that a square-like target droplet enhances both accuracy and consistency.

In Fig. 5c, target droplets possess a unified size of D_1 = 8 with two morphologies (2×4, 4×2). Reservoir droplets possess a unified size of D_2=248 with two morphologies (31×8, 8×31). Failed splits occur under D_1 = 4×2 while D_2 = 8×31, at motion modes (-1,0).and (-1,1). The highest accuracy and consistency occur under D_1 = 2×4 and D_2 = 31×8 at motion mode (-1,0), where $|D_{t-exp}.ND|$=0.006, CV = 0.039. It emerges under the same condition for generating 1.5625% target droplet in D = 1024 scenario (Fig. 5e), where the shapes of the two sub-droplets remain unchanged, and sizes halved. Similarly, the failed splitting scenario is consistent with that of generating 1.5625% target droplet in D = 1024. It demonstrated that geometric compatibility governs squeezing performance, and that optimal conditions scale with droplet size, confirming that shape ratios rather than absolute dimensions determine splitting feasibility and accuracy.

Figure 5d shows target droplets D_t=4 (2×2) of the ratio 1.5625% out of an initial droplet D = 256 at sub-droplet motion (0,1), splits only succeeded under motion mode (0,1); all splits at motion modes (-1,0) and (-1,1) failed. The highest accuracy and consistency occur under D_1 = 2×2 and D_2 = 16×16 at motion mode (-1,0), where $|D_{t-exp}.ND|$=0.03, CV = 0.047. Comparison of the optimal conditions across Figs. 5b, 5c, and 5d reveals that as the target ratio decreases from 3.125% to 1.5625%, both |D□_□□□.ND| and CV increase (from 0.006 to 0.03 and from 0.039 to 0.047, respectively), indicating that ultra-low-ratio splitting compromises accuracy and consistency. Mode (0,1) becomes the only viable option at the lowest ratio, suggesting a narrowing operational window as resolution pushes extreme limits.

In Fig. 5e, target droplets possess a unified size of D_1 = 32 with four morphologies (2×16, 4×8, 8×4, 16×2). Reservoir droplets possess a unified size of D_2=992 with three morphologies (31×32, 62×16, 16×62). As $D_{t-exp}.ND < -0.5$ indicates that accuracy < 50%, it can be regarded as failed splitting. Failed splits occur under D_1 = 16×2 and D_2 = 62×16 at all motion modes, and while D_1 = 2×16 and D_2 = 62×16 at (-1,0).and (-1,1). Overall intra-consistency is enhanced, compared to all previous squeezing results. Several trends are observed. First, regardless of the sizes of both sub-droplets, all target droplets D_{t-exp}.ND show an increasing trend as motion modes (Dm_1, Dm_2) change from (-1,0), to (-1,1), and to (0,1). Second, ole movement of the target droplet yields undersized target droplets, while sole movement of the reservoir droplet yields oversized ones. Third, motion mode (0,1) exhibits the highest feasibility, enabling splitting across a broader range, however with excessive D_{t-exp}.ND. Meanwhile, simultaneous movements of both sub-droplets slightly enhance target accuracy. Failed splitting occurs when the geometric ratio of both sub-droplets exceeds certain limit.

In conclusion, squeezing enables ultra-low-ratio droplet generation down to 1.5625%, but with an inherent trade-off between resolution and precision; success is governed by geometric compatibility, with orthogonal elongation mismatch as a universal failure mechanism, while motion mode (0,1) offers the broadest feasibility at the cost of larger errors, and larger absolute droplet sizes improve reproducibility.

(a) Schematic diagram of squeezing. (b). Statistical analysis on initial droplet D = 1024 and target droplet D_t=16, where D_t%=1.5625%, with different sub-droplets shapes at sub-droplets motion modes (-1,0), (1,1) and (0,1). (c) Statistical analysis on initial droplet D = 256 and target droplet D_t = 4, where D_t%=1.5625%. (d) Statistical analysis on initial droplet D = 256 and target droplet D = 8, where D_t%=3.125%. (e) Statistical analysis on initial droplet D = 1024 and target droplet D = 32, where D_t%=3.125%.

Sequential splitting decision process for ultra-low-ratio sub-droplet generation

A flow chart for generating optimal multi-step droplet splitting sequences from a given initial droplet to a target droplet is demonstrated, aiming at precise generation for ultra-low-ratio sub-droplet (Fig. 6). A systematic multi-step droplet splitting algorithm driven by cumulative accuracy and volume ratio constraints is proposed to enable automated target droplet generation (Fig. 6a). Computational procedures proceed as follows:

First, input parameters are initialized, comprising the initial droplet size D, target droplet volume D_t, and constraints including required cumulative splitting accuracy Acc and other relative conditions, such as steps, electrode array scale, etc. Then, cumulative splitting ratio planning is performed. Overall target volume ratio is calculated and decomposed into a series of cascaded stepwise splitting ratios, where cumulative product equals the final target ratio. Cumulative accuracy constraint is applied. A single-step splitting accuracy threshold is set to ensure that the total multi-step cumulative error remains below the target accuracy Acc. Following exhaustive solution generation, optimal splitting mode selection is conducted. Based on the splitting ratio, droplet size, shape, and accuracy requirements, the most accurate or efficient splitting scheme is determined from symmetric splitting, asymmetric splitting, deformative splitting, and squeezing. A multi-step splitting sequence is then constructed from experimental data. The electrode activation order and timing are determined; stepwise droplet splitting is executed. The volume ratio and accuracy of each step are recorded; and the cumulative splitting ratio and cumulative accuracy are updated iteratively until convergence to the target specifications is verified. Finally, the output scheme is generated, comprising the complete multi-step splitting steps, electrode activation layout and driving timing, as well as the final cumulative splitting ratio and cumulative splitting accuracy.

To validate the feasibility of the proposed droplet splitting decision diagram, a case study of generating a target droplet D_t=8 from the initial droplet D = 1024 is investigated. Here the actual volume of the target

droplet is 12 nL. The accumulative target ratio is 0.78125%, below the minimal ratio of a single split. Hence, multi-step splitting can enable droplet splitting in extremely low ratio. Here potential two-step splitting solutions are presented (Fig. 7b), where $D_t\%=D_{t1}\%\ D_{t2}\%$. The optimal sub-droplets motion patterns and shapes are searched from the experimental results from previous sections. The cumulative target droplet accuracy and CV are illustrated in Fig. 7c. Cumulative accuracy is defined as the product of accuracies of step 1 and 2, as shown in the grouped column figure. Cumulative CV is defined as the arithmetic square root of CV of step 1 and 2, as shown in the stacked column figure. Consequently, the cumulative results among the 6 solutions are compared. Group 1 exhibits the poorest accuracy of 1.31963. In this configuration, step 1 employs asymmetric splitting, where D_1 = 32×16, D_2 = 32×16, $D_{t1}\%$=50%, at mode (-1,1). Step 2 employs deformative splitting, where D_1 = 4×2, D_2 = 21×24, $D_{t2}\%$=1.5625%, at mode (-1,0). Group 4 exhibits the optimal accuracy of 1.05868. In this configuration, step 1 employs asymmetric splitting, where D_1 = 2×16, D_2 = 62×16, $D_{t1}\%$=3.1252%, at mode (0,1). Step 2 employs deformative splitting, where D_1 = 4×2, D_2 = 4×6, $D_{t2}\%$=25%, at mode (1,1). Excessive error accumulates when an ultra-low-ratio step follows a high-ratio split, demonstrating that balanced ratio allocation across steps is more critical than minimizing any individual step ratio. Optimal multi-step accuracy further requires motion modes validated for each ratio range and geometric continuity between steps.

(a) Flowchart of the multi-step droplet splitting scheme driven by cumulative accuracy and splitting ratio. (b) 6 possible experimental solutions of generating D_t=8 out of D = 1024. (c) The cumulative results of 6 solutions, including the grouped column figure of accuracies and stacked column figure of CV.

Conclusion

To summarize, this work conducted a precise sub-droplet splitting study based on the large-scale AM-DMF platform. Quantitative performance boundaries of four droplet splitting strategies—symmetric splitting, asymmetric splitting, deformative splitting, squeezing, are systematically characterized. The results reveal that splitting accuracy, feasibility, and achievable minimum droplet ratio are governed by four primary factors: initial droplet size and shape, splitting ratio, sub-droplet motion mode, and the geometric relationships between sub-droplets. The optimal splitting modes have been discovered. Notably, a geometric ratio threshold exists, beyond which splitting invariably fails, regardless of the strategy employed. Based on quantitative insights, a constraint-driven optimal sequential splitting decision framework that generates multi-step splitting sequences from experimental data is proposed. The framework successfully enables ultra-low-ratio droplet generation (e.g., 0.78125%) that is unattainable by any single-step method, with a cumulative accuracy of 1.05868 and a cumulative CV of 0.024, upon a target droplet of 12nL.

This work provides a theoretical and technical foundation for customizable, high-precision, multi-step microdroplet generation in digital microfluidics. In the future, the proposed platform will enable further studies on high-resolution droplet generation for digital bioassays, integrated multi-step sample

preparation workflows, and adaptive splitting strategies driven by real-time feedback. Bioassays, including high-throughput single-cell analysis, personalized medicine assays, etc. that require precise, customizable multi-step droplet generation are promising to be developed on the DMF platform.

Methods

AM-DMF chip design and Equipment

The AM-DMF chip was designed and packaged by ACX Instruments Ltd. (Cambridge, UK) and Guangdong ACXEL Micro & Nano Tech Co., Ltd. (Foshan, China). The DMF chips comprised a top ITO-glass plate and a bottom active-matrix electrode array plate. The scale of the pixel electrode array is 128×128, featuring 16,384 independently controlled electrodes. The electrode pitch was 250 μm, and the plate gap was 50 μm. The theoretical volume of a single electrode droplet is 3.125 nL. The equipment used to support the AM-DMF chip was DM Lite™ with a DM ctrl™ software interface (ACX Instruments Ltd. and Guangdong ACXEL Micro Nano Tech Co., Ltd.). It consists of a core development board, AM-DMF (AMPixel™) biochips, an optical detection camera.

Declarations

Funding:

H. M. acknowledge funding from the National Natural Science Foundation of China (T2541056). C. H acknowledges funding from the Basic Research Program of Suzhou, China (No. SSD2025014).

Author contributions

C.H. and H.M. conceived the study and conceived the projects. C.H. performed the experiments, analyzed the data, and wrote the paper.

References

1. Whitesides, G.M., *The origins and the future of microfluidics*. nature, 2006. 442(7101): p. 368–373.
2. Joensson, H.N. and H. Andersson Svahn, *Droplet Microfluidics—A Tool for Single-Cell Analysis*. Angewandte Chemie International Edition, 2012. 51(49): p. 12176–12192.
3. Macosko, Evan Z., et al., *Highly Parallel Genome-wide Expression Profiling of Individual Cells Using Nanoliter Droplets*. Cell, 2015. 161(5): p. 1202–1214.
4. Yafia, M., et al., *Microfluidic chain reaction of structurally programmed capillary flow events*. Nature, 2022. 605(7910): p. 464–469.
5. Paratore, F., et al., *Reconfigurable microfluidics*. Nat Rev Chem, 2022. 6(1): p. 70–80.

6. Zhu, P. and L. Wang, *Passive and active droplet generation with microfluidics: a review*. Lab on a Chip, 2017. 17(1): p. 34–75.
7. Huang, K., et al., *A high-precision nanoliter droplet dispensing system based on optoelectrowetting with tunable droplet volume*. Microsystems & Nanoengineering, 2025. 11(1): p. 231.
8. Wang, Y., et al., *Pick-up single-cell proteomic analysis for quantifying up to 3000 proteins in a Mammalian cell*. Nature Communications, 2024. 15(1): p. 1279.
9. Wang, X., et al., *Data-Driven Theoretical Modeling of Centrifugal Step Emulsification and Its Application in Comprehensive Multiscale Analysis*. Advanced Science, 2025. 12(13): p. 2411459.
10. Pollack, M.G., R.B. Fair, and A.D. Shenderov, *Electrowetting-based actuation of liquid droplets for microfluidic applications*. Applied Physics Letters, 2000. 77(11): p. 1725–1726.
11. Fair, R.B., *Digital microfluidics: is a true lab-on-a-chip possible?* Microfluidics and Nanofluidics, 2007. 3: p. 245–281.
12. Cho, S.K., H. Moon, and C.-J.C. Kim, *Creating, transporting, cutting, and merging liquid droplets by electrowetting-based actuation for digital microfluidic circuits*. IEEE\/ASME Journal of Microelectromechanical Systems, 2003. 12: p. 70–80.
13. Yu, X., et al., *Digital microfluidics-based digital counting of single-cell copy number variation (dd-scCNV Seq).* Proceedings of the National Academy of Sciences, 2023. 120(20): p. e2221934120.
14. Ng, A.H.C., et al., *A digital microfluidic system for serological immunoassays in remote settings*. Science Translational Medicine, 2018. 10(438): p. eaar6076.
15. Ma, H., et al., *Large-area manufacturable active matrix digital microfluidics platform for high-throughput biosample handling*. 2020. 35.5.1–35.5.4.
16. Wang, D., et al., *Active-matrix digital microfluidics for high-throughput, precise droplet handling*. Nature Reviews Electrical Engineering, 2026. 3(1): p. 46–60.
17. Jia, Z., et al., *Artificial intelligence-enabled multipurpose smart detection in active-matrix electrowetting-on-dielectric digital microfluidics*. Microsystems & Nanoengineering, 2024. 10.
18. Guo, Z., et al., *Deep Learning-Assisted Label-Free Parallel Cell Sorting with Digital Microfluidics*. Advanced Science, 2025. 12(1): p. 2408353.
19. Hu, C., K. Jin, and H. Ma, *A universal model for continuous "one-to-two" high-efficient droplet generation in digital microfluidics*. Applied Physics Letters, 2023. 122(18).
20. Hu, C., et al., *A geometrical model of pinch-off in digital microfluidics underpins "one-to-three" droplet generation*. Applied Physics Letters, 2022. 120(12).
21. Hu, C., et al., "*Cell-On-Demand" Digital Microfluidics for Real-Time Low-Abundance Single-Cell Isolation and Sample Analysis*. Small, 2025. 21(31): p. 2504239.

Figures

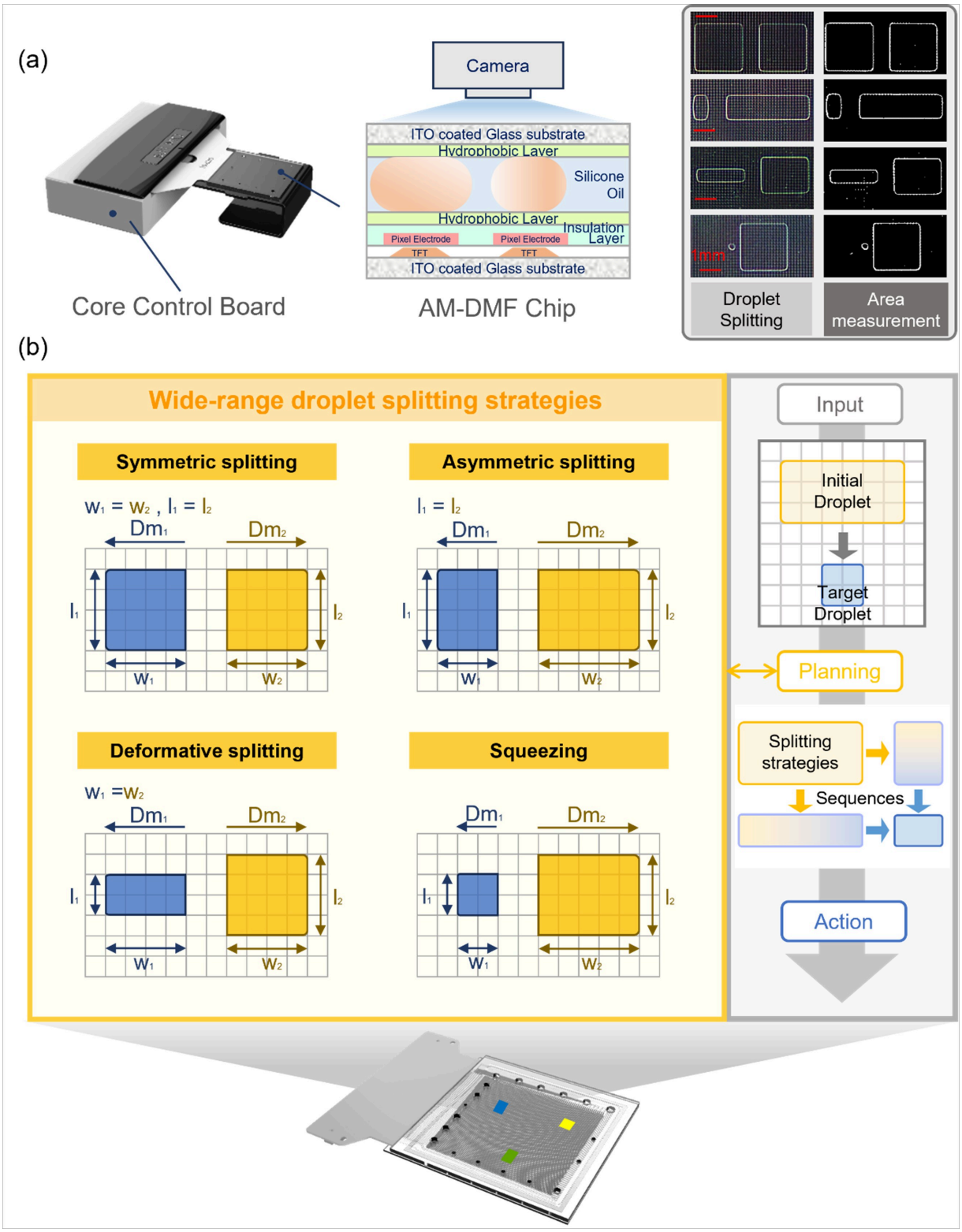


Figure 1

Schematic of droplet splitting studies on AM-DMF chip

(a) System setup, chip structure and optical detection images. (b) Schematic of four different droplet splitting strategies on AM-DMF (symmetric splitting, asymmetric splitting, deformative splitting, squeezing). A framework for optimal target droplet splitting decision is also established.

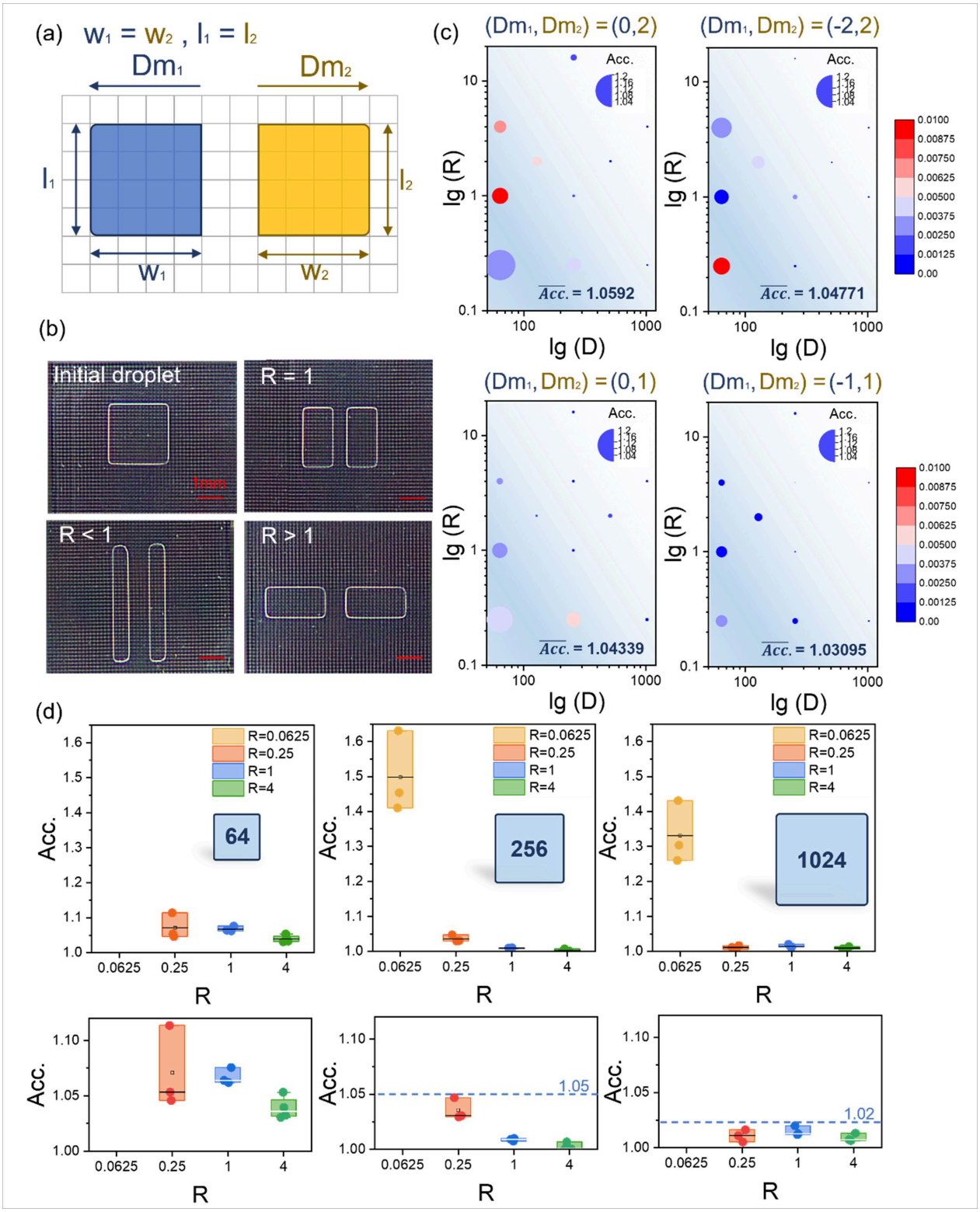


Figure 2

Symmetric droplet splitting.

(a) Schematic diagram of symmetric splitting. (b) Experimental images of symmetric splitting. Scale bar is 1mm. (c) Experimental results of sub-droplet accuracy at different splitting motion modes (Dm_1, Dm_2),

initial droplet size (D=w l) and shape (R=w/l). (d) Sub-droplet accuracies under three typical initial droplet sizes (D=64, 256, 1024) when motion mode (Dm_1, Dm_2) = (-1,1).

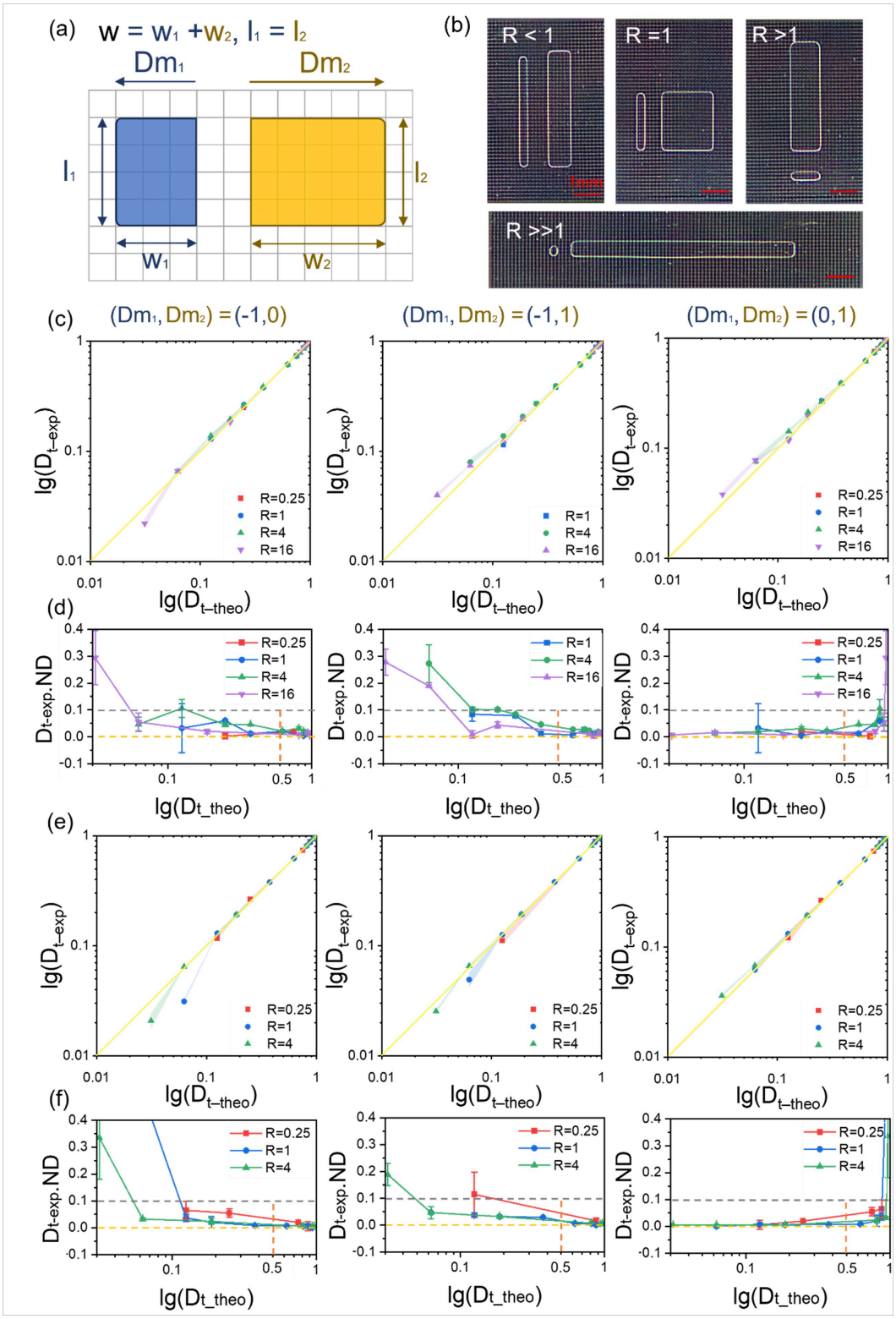


Figure 3

Asymmetric droplet splitting

(a) Schematic diagram of asymmetric splitting. (b) Experimental images of deformative splitting in varying initial droplet shapes. (b) Correlation analysis on initial droplet D=256 with different shapes R under sub-droplets motion modes (Dm_1, Dm_2) = (-1,0), (-1,1) and (0,1). (c) Correlation analysis on initial droplet sizes D= 256 and (e) D=1024 with different shapes R under three motion modes. (d) Statistical analysis on the absolute normalized deviation of experimental results of target droplet ratio ($|D_{t_exp}.ND|$) in relation with corresponding theoretical target droplet ratio (D_{t_theo}) under initial droplet sizes D= 256 and (f) D=1024.

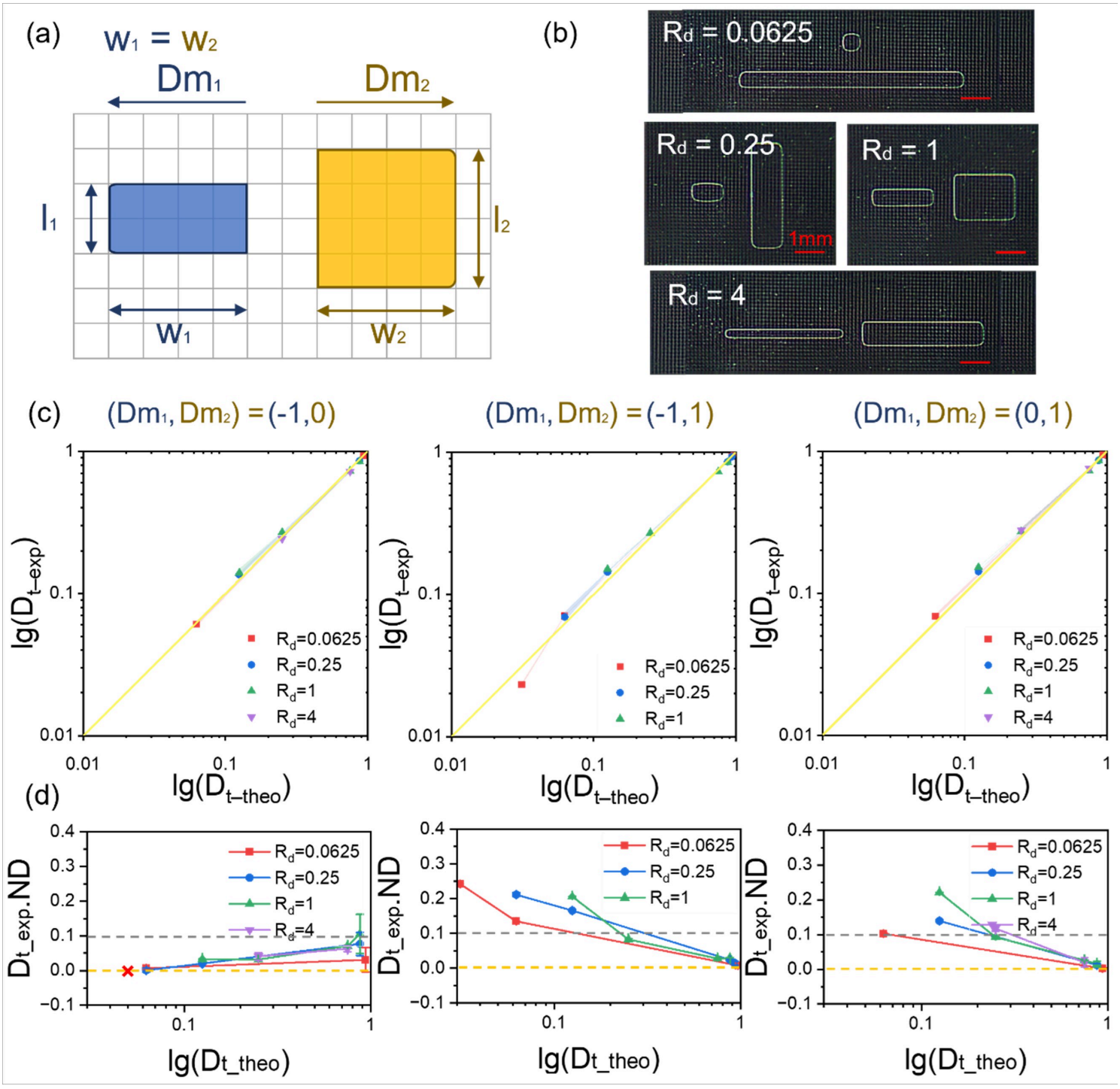


Figure 4

Deformative splitting

(a) Schematic diagram of deformative splitting. (b) Experimental images of deformative splitting in varying R_d. (c) Correlation analysis and on initial droplet sizes D=256 with varying shapes R_d. at different sub-droplets motion modes (Dm_1, Dm_2) = (-1,0), (-1,1) and (0,1). (d) Statistical analysis on absolute normalized deviation of experimental results of target droplet ratio ($|D_{t_exp}.ND|$) in relation with corresponding theoretical target droplet ratio (D_{t_theo}) when D=256.

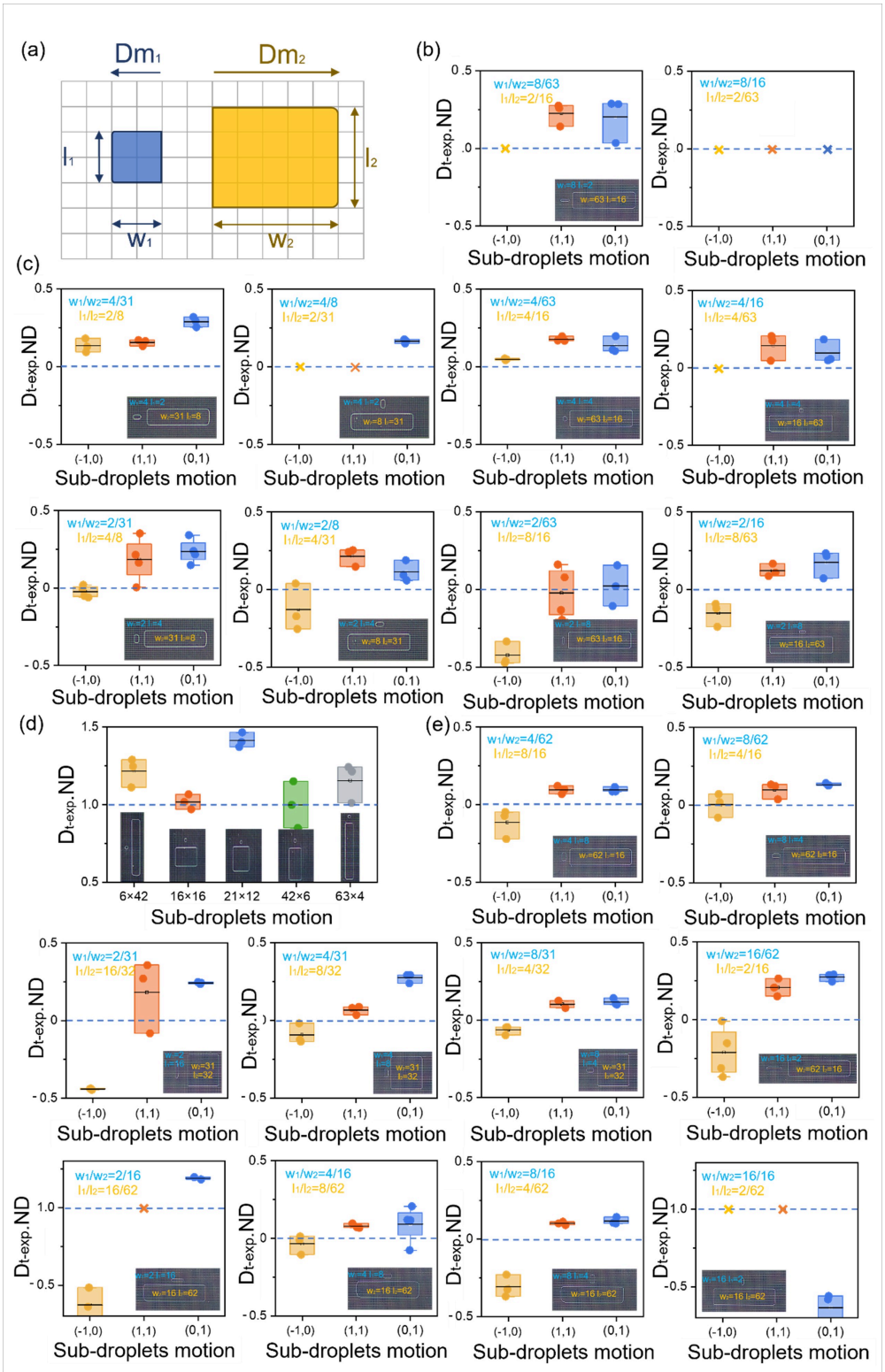


Figure 5

Squeezing

(a) Schematic diagram of squeezing. (b). Statistical analysis on initial droplet D=1024 and target droplet D_t=16, where D_t%=1.5625%, with different sub-droplets shapes at sub-droplets motion modes (-1,0), (1,1) and (0,1). (c) Statistical analysis on initial droplet D=256 and target droplet D_t = 4, where D_t%=1.5625%.

(d) Statistical analysis on initial droplet D=256 and target droplet D=8, where D_t%=3.125%. (e) Statistical analysis on initial droplet D=1024 and target droplet D=32, where D_t%=3.125%.

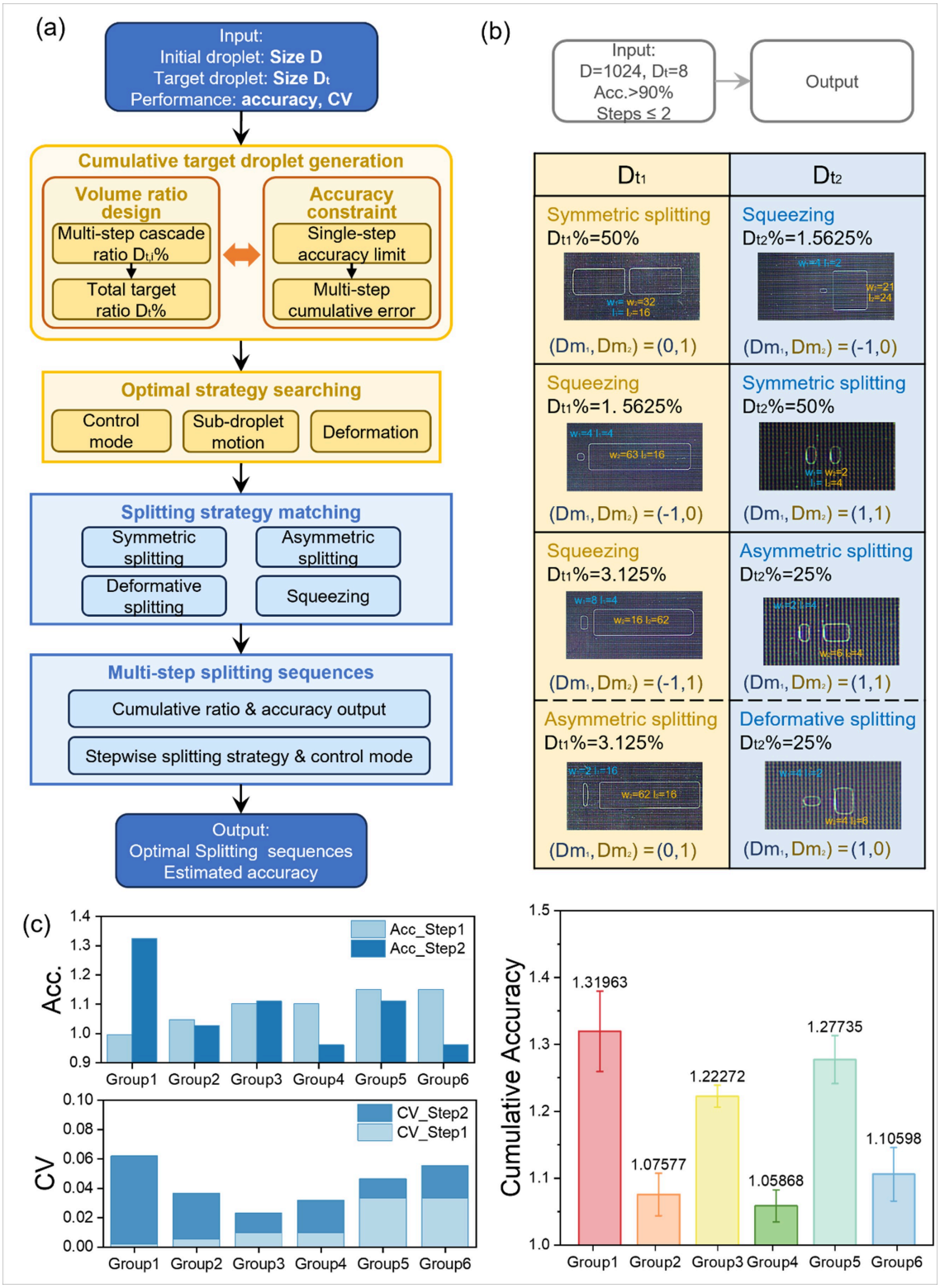


Figure 6

Sequential droplet generation decision process and applications

(a) Flowchart of the multi-step droplet splitting scheme driven by cumulative accuracy and splitting ratio. (b) 6 possible experimental solutions of generating D_t=8 out of D=1024. (c) The cumulative results of 6 solutions, including the grouped column figure of accuracies and stacked column figure of CV.